The Response of the North Pacific Ocean to Decadal Variability in Atmospheric Forcing: Wind versus Buoyancy Forcing*

LuAnne Thompson

School of Oceanography, University of Washington, Seattle, Washington

Carol A. Ladd

NOAA/Pacific Marine Environmental Laboratory, Seattle, Washington

ABSTRACT

Both wind and buoyancy forcing result in variability in the North Pacific Ocean thermocline. A vertical modal analysis of the density deviations in a 30-yr run of an ocean general circulation model of the North Pacific forced by atmospheric variability is used to identify the spatial and temporal patterns of the different baroclinic modes. The different dynamic vertical modes show distinct propagation characteristics, with the first baroclinic mode exhibiting consistent westward propagation at all latitudes. The higher baroclinic modes show westward phase propagation at low latitudes but propagate eastward at higher latitudes. The propagation characteristics of each mode can be understood by the inclusion of the zonal mean flow in the vertical structure equation. Evaluation of the Ekman pumping and diapycnal fluxes in the quasigeostrophic potential vorticity equation for each dynamic vertical mode distinguishes their effects on the thermocline variability. Wind variability dominantly forces the first baroclinic mode response while buoyancy forcing results in a higher baroclinic mode response. Two additional numerical model runs, one with climatological wind stress and one with climatological heat fluxes and SST, demonstrate the relative roles of Ekman pumping and diabatic pumping on the forcing of each vertical mode. Ekman pumping is important throughout the North Pacific for forcing first-mode variability. Diabatic pumping, or that associated with thermal forcing, is important in the Kuroshio Extension and much less so farther to the south and can act to suppress the first-baroclinic-mode Ekman pumping response. The second baroclinic mode has a band of positive energy emanating westward from the eastward end of the Kuroshio Extension and ending at the western boundary at 20°N, reflecting the strong effect of the mean flow on wave propagation of the higher baroclinic modes. Mode coupling also occurs, especially in the westward return flow of the subtropical gyre. The results are shown to be consistent with the one-dimensional wave equation and show the importance of inclusion of the first several baroclinic modes in studies of the decadal variability in the ocean.

1. Introduction

The North Pacific Ocean shows evidence of inter-annual to decadal fluctuations with a remarkable regime shift occurring in 1976. This variability in the ocean has been termed the Pacific decadal oscillation (PDO; Mantua et al. 1997). Mantua et al. define a PDO index as the time series of the leading EOF of sea surface temperature (SST) in the North Pacific. Although this time series is correlated with the leading EOF of North Pacific sea level pressure (SLP), it is not clear if it results from a coupled ocean–atmosphere mode or purely a passive response of the ocean to atmospheric forcing (Frankignoul et al. 1997).

There are several mechanisms that have been proposed that could initiate a coupled ocean–atmosphere response with the midlatitude ocean playing an active role. Gu and Philander (1997) suggest that temperature anomalies in midlatitudes could be subducted and subsequently advected to the equatorial thermocline where they would then influence tropical SSTs. This would result in changes in the midlatitude wind field from atmospheric teleconnections from the Tropics. While evidence for atmospheric teleconnections is strong (Zhang et al. 1997), the evidence for the oceanic connection is less compelling. In addition, Gu and Philander (1997) ignore the dynamic influence of buoyancy forcing on the thermocline. Deser et al. (1996) show that temperature anomalies can be traced from midlatitudes

Corresponding author address: Dr. LuAnne Thompson, School of Oceanography, Box 355351, University of Washington, Seattle, WA 98195.
E-mail: luanne@ocean.washington.edu

through different pentads, and Schneider et al. (1999) showed that these anomalies do not penetrate farther south than 18°N and that local winds in the Tropics are more important for determining thermocline depth anomalies there. Last, coupled ocean–atmosphere simulations of Latif and Barnett (1994 and 1996) demonstrate a midlatitude-only coupled mode. In the coupled mode, increased advection in the Kuroshio generates warm temperature anomalies in the Kuroshio Extension. This results in a reduction in the zonal wind stress, and latent heat flux to the atmosphere. The subtropical gyre then adjusts to changes in the wind, mediated by first baroclinic mode long Rossby waves. The transport in the Kuroshio then decreases, resulting in a negative temperature anomaly providing the negative feedback. In support of this mechanism, Deser et al. (1999) show that the transport of the Kuroshio is lag correlated with wind curl, suggesting a delayed Sverdrup response. In more recent analysis of coupled ocean models, Schneider et al. (2002) show that there is evidence that first-baroclinic-mode Rossby waves carry thermocline depth purturbations to the west, which then results in a shift of the Kuroshio Extension and results in SST anomalies. While they show evidence for a positive feedback between the coupled model Kuroshio Extension SST and the North Pacific Ekman pumping, which is consistent with a 20–30-yr period, no negative feedback was found as was suggested by Latif and Barnett (1994). This does, however, lead to an ability to predict SSTs in the Kuroshio Extension region with a lead time of up to three years (Schneider and Miller 2001).

In each of the above scenarios, changes in atmospheric forcing result in an oceanic response in the thermocline: either temperature/salinity anomalies within the thermocline forced by changes in buoyancy forcing (Gu and Philander 1997) or adjustment of the circulation to changes in Ekman pumping through the propagation of long Rossby waves (Latif and Barnett 1996). While the local adjustment of the ocean to changes in surface forcing and the remote adjustment by first-baroclinic-mode Rossby waves has been shown to be important in the ocean thermodynamics (see, i.e., Seager et al. 2001), higher-mode Rossby waves dynamics have been ignored in the context of realistic coupled or ocean-only models. However, Liu (1999a) investigated the response of the ocean to forcing by Ekman pumping and buoyancy forcing. He finds that each type of forcing initiates a different response in the thermocline. Ekman pumping generates a response similar to the first baroclinic mode in a resting ocean and the resulting anomaly has westward phase propagation. Buoyancy forcing generates a response that has similar vertical structure to the second baroclinic mode but follows an ''advective'' pathway, following the flow field of the midthermocline. In a 2½-layer model, the first baroclinic mode describes thermocline heave, while the second baroclinic mode describes the thickening and thinning of the thermocline. While Liu (1999) demonstrated that an idealized ocean

does respond with these two modes, the relationship between the actual atmospheric forcing and the response of these two modes of variability needs to be clarified. In addition, the role of higher vertical modes was not explored.

In this study we use a vertical modal decomposition of a North Pacific Ocean model simulation of decadal variability to investigate the amplitudes and spatial structure of the baroclinic modes and their respective forcing fields to sort out the mechanisms that control the oceanic response on decadal time scales. To do this we use the approach of Thompson et al. (2002), doing a vertical modal decomposition of isopycnal displacements of a numerical model. The model run used is the one described by Ladd and Thompson (2002), a 30-yr simulation of the North Pacific that was used to examine the decadal scale changes in the central mode water (CMW), the subtropical mode water that forms in the central Pacific. An outline is as follows: we first review the decomposition method of Thompson et al. (2002), with the addition of the background mean flow. We then apply it to the wintertime anomalies of the model. The propagation characteristics of each mode are examined, followed by a discussion of the forcing fields projected onto the potential vorticity equation of each mode. The results are then interpreted using the one-dimensional Rossby wave equation. Mode coupling is then discussed. Last, the consequences for understanding coupled ocean–atmosphere modes of variability are explored.

2. Model formulation

The model used for this study is the Hallberg Isopycnal Model (Hallberg and Rhines 1996; Hallberg 2000; Ladd and Thompson 2001, 2002; Thompson et al. 2002). It is configured with 16 layers in the vertical, including a Kraus–Turner bulk mixed layer and a variable density buffer layer. The model domain is 20°S–60°N, 126°E–76°W, with a 2° horizontal resolution. Mixed layer densities and isopycnal layer thicknesses were initialized with sea surface densities and layer thicknesses calculated from Levitus climatological September temperature and salinity values. After an initial 30-yr spinup using climatological forcing, the model was forced at the surface with daily linear interpolations of monthly heat fluxes, climatological freshwater flux (converted to density flux) and surface winds from January 1965 to December 1993. There is also a weak relaxation of mixed layer densities to observed values (35 days for a 100-m mixed layer). It is the same model run as discussed in Ladd and Thompson (2002). Model diagnostics include the cumulative diapycnal volume flux across each layer interface.

3. Modal decomposition

To understand the dynamic response of the model ocean to variability in atmospheric forcing, we use a

vertical modal decomposition of density structure (interface displacements). Dynamic vertical modes form a complete orthogonal set that can describe any perturbations of density. We follow the procedure of Thompson et al. (2002) where an analysis of the seasonal cycle of thermocline displacement was performed, and we summarize the method below. Here we use the mean winter stratification field as the mean density field and take the winter anomalies from this mean, allowing us to ignore seasonal thermocline changes and to focus on interannual changes. The higher-frequency signals are primarily at the annual period, and, since we are sampling at the same time of year every year, we are looking at the anomaly from the seasonally generated Rossby waves. The seasonal Rossby waves have larger amplitude than the interannual signal [see Thompson et al. (2002) for more details about the higher-frequency signal].

We made two simplifying assumptions in this analysis. First, we assumed that linearization is appropriate. Linearization requires that interface deviations be small in comparison with the mean layer thicknesses and is probably a valid approximation for interannual time scales. Second, we assumed the Wentzel–Kramers–Brillouin (WKB) approximation can be made, allowing the analysis to be done independently at each location. The requirement for this approximation is that the background state changes over a length scale that is large in comparison with the wavelength of the perturbations. The mean stratification in the ocean changes relatively slowly and has basin scale, while the perturbations have somewhat shorter length scales, making the approximation marginally valid. Despite that, the success of the analysis for the seasonal cycle shows that this method is useful for giving a dynamical interpretation of the ocean's response to atmospheric forcing variability (Thompson et al. 2002). The WKB approximation in the context of topographic variations is justified by the work of Killworth and Blundell (1999). They argue that while the presence of topographic slopes does impact the local baroclinic modes and their phase speeds, in a basinwide average, topographic variations do not influence the overall propagation characteristics of the long-wavelength Rossby waves.

a. Formalism

To perform the analysis, the vertical structure equation is derived in a layered framework. A modal decomposition is done and then the quasigeostrophic potential vorticity equation is used to diagnose the impact of Ekman pumping versus diabatic forcing on thermocline variability.

In the absence of mean flow, the potential vorticity equation in an interior layer for motions with length scales much larger than the deformation radius can be written

$$\frac{\partial}{\partial t}\left[\frac{(\psi_n - \psi_{n+1})}{H_n g_n} + \frac{(\Psi_n - \Psi_{n-1})}{H_n g_{n-1}}\right] + \beta\frac{\partial \Psi_n}{\partial x} = 0. \quad (1)$$

Here, ψ_n is the streamfunction in layer n, H_n is the mean thickness of layer n, and g_n the reduced gravity between layer n and layer $n + 1$. The top and bottom layers are modified from this equation to include the effects of friction and atmospheric forcing [see (10)–(12) of Thompson et al. (2002)]. The resulting motions satisfy a nondispersive wave equation. The dispersion relation and vertical structure of wave motions can be found from the layered version of the vertical structure equation as follows:

$$\frac{\phi_1 - \phi_2}{H_1 g_1} + \frac{\phi_1}{H_1 g} + \frac{1}{c^2}\phi_1 = 0 \quad (2)$$

for the top layer,

$$\frac{\phi_n - \phi_{n+1})}{H_n g_n} + \frac{(\phi_n - \phi_{n-1})}{H_n g_{n-1}} + \frac{1}{c^2}\phi_n = 0 \quad (3)$$

for the nth interior layer, and

$$\frac{(\phi_m - \phi_{m-1})}{H_m g_{m-1}} + \frac{1}{c^2}\phi_m = 0 \quad (4)$$

for the bottom layer, where m is the number of layers, c is the gravity wave speed, and ϕ_n is the vertical structure of the streamfunction for the nth vertical mode. In this framework, the streamfunction is related to interface displacements by

$$f\phi_n = g\hat{h}_0 + \sum_{i=1}^{n-1} g_n\hat{h}_n. \quad (5)$$

Here $\hat{h}_n$ is the interface displacement of the bottom of layer n from its mean position. Long Rossby waves then have phase speed $C = -\beta c^2/f^2$, which is always westward.

In matrix notation, (2)–(4) can be written

$$\mathbf{L}\Phi = -\frac{1}{c^2}\Phi. \quad (6)$$

Here $\mathbf{L}$ is a matrix containing the operators in the first two terms of (2) and (3) and the first term in (4) and Φ is a vector containing the vertical structure of the streamfunction for a particular mode. Equation (6) is solved as an eigenvalue problem for $-c^{-2}$. The eigenvectors are sorted by their phase speeds, with the most rapid phase speed being the barotropic mode. The phase speed of the first-baroclinic-mode gravity wave shows reasonable correspondence with other calculations.

The effects of the vertical shear on the modal structure and phase speeds can be ignored as long as the phase speed of the wave is much greater than the mean flow velocity. According to the calculations of Killworth et al. (1997), the first baroclinic modal structure is relatively uninfluenced by the zonal vertical shear, although the phase speed can differ from the zero mean flow

phase speed by as much as factor of 2. For the higher vertical modes, one would expect that the vertical structure depends on the mean flow speed, especially where the mean flow is large.

To test this, we included the mean flow in the modal analysis. When the (winter) mean flow is included, several things change in the system: it is no longer self-adjoint, the eigenfunctions are no longer complete, and instabilities are possible (Killworth et al. 1997). In a layered framework in an interior layer, the potential vorticity equation becomes

$$
\frac{\partial}{\partial t}\left(\frac{\phi_{n+1} - \phi_n}{H_n g_n} + \frac{\phi_{n-1} - \phi_n}{H_n g_{n-1}}\right)
$$
$$
+ U_n \frac{\partial}{\partial x}\left(\frac{\phi_{n+1} - \phi_n}{H_n g_n} + \frac{\phi_{n-1} - \phi_n}{H_n g_{n-1}}\right)
$$
$$
+ V_n \frac{\partial}{\partial y}\left(\frac{\phi_{n+1} - \phi_n}{H_n g_n} + \frac{\phi_{n-1} - \phi_n}{H_n g_{n-1}}\right)
$$
$$
+ \frac{\partial \phi_n}{\partial x}\left(\beta + \frac{U_{n+1} - U_n}{H_n g_n} + \frac{U_{n-1} - U_n}{H_n g_{n-1}}\right)
$$
$$
+ \frac{\partial \phi_n}{\partial y}\left(\frac{V_{n+1} - V_n}{H_n g_n} + \frac{V_{n-1} - V_n}{H_n g_{n-1}}\right) = 0. \tag{7}
$$

If only zonal mean flow occurs, then the potential vorticity eigenvalue problem reduces to

$$
(U_n - C)\left(\frac{\phi_{n+1} - \phi_n}{H_n g_n} + \frac{\phi_{n-1} - \phi_n}{H_n g_{n-1}}\right)
$$
$$
+ \phi_n\left(\beta - \frac{U_{n+1} - U_n}{H_n g_n} + \frac{U_{n-1} - U_n}{H_n g_{n-1}}\right) = 0. \tag{8}
$$

If we only include the zonal mean flow and the eigenvalues are sorted correctly, the lower vertical modes can be identified with the resting vertical modes. Since the flow can be unstable in the southern return flow of the subtropical gyre, we use only the real parts of the phase speed. After removing the barotropic mode, the rest of the modes are sorted by the amplitude of their real phase speeds.

The vertical structure for the first baroclinic mode is insensitive to the presence of the mean flow (Fig. 1), as found by Killworth et al. (1997). The phase speed for the first baroclinic mode follows the predictions of Killworth et al. with an increase of the phase speed at midlatitudes with the inclusion of the mean flow. In our calculation, the phase speed increases by about 30% at midbasin. In the eastern basin, the increase is smaller (Fig. 2). The average phase speed between 35° and 40°N is estimated as 2.0 cm s^{-1} for a resting ocean and 2.3 cm s^{-1} when the mean zonal flow is included. This compares well with the estimate of 2.5 cm s^{-1} of Schneider and Miller (2001) that they used in their one-dimensional wave equation model that is used to estimate

SSTs in the Kuroshio Extension. Surprisingly, the second-baroclinic-mode structure is also relatively insensitive to the mean flow structure. While this is not true everywhere in the gyre, for much of the gyre the vertical structure is reasonably well represented by the resting vertical structure. The second-baroclinic-mode phase speed is greatly influenced by the presence of the mean flow. In the Kuroshio Extension the corrected phase speed becomes eastward because the resting Rossby wave phase speed is not large enough to overcome the mean flow. In a more complete analysis, Killworth and Blundell (2001) derive shear modes in a continuously stratified fluid in which the vertical structure of the mean flow is projected onto the resting vertical modes. They show that the first baroclinic shear mode is very much like the resting first mode, while the second mode can be very much changed. They suggest that there may be coupling or leakage from the faster first shear mode to the second shear mode in some regions of the gyre. They associate this second mode with Liu's (1999a,b) advective mode as described above. There is potentially large coupling between the first two modes, especially in the return flow of the subtropical gyre. We will discuss this more in section 6.

Killworth et al. (1997) showed that, when only zonal mean flow is present and the mean flow is much smaller than the phase speed, a correction to the resting phase speed can be estimated. The correction depends on the unperturbed vertical structure, the mean flow, and the mean shear. The wave remains nondispersive in this approximation. The dispersion relation can then be written

$$
\omega_n = k\left(-\beta \frac{c_n^2}{f_0^2} + A_n\right), \tag{9}
$$

where A_n depends on the zonal velocity, the vertical shear, and the vertical structure of the nth baroclinic mode. When both zonal and meridional mean flows are included, the flow is no longer nondispersive. If the mean flow is small in both directions, then, following the formulation of Killworth et al. (1997), the dispersion relation can be written

$$
\omega_n = k\left(-\beta \frac{c_n^2}{f_0^2} + A_n\right) + lB_n, \tag{10}
$$

where similarly B_n depends on the meridional velocity and its vertical shear as well as the vertical structure of the nth baroclinic mode. Under this approximation wave characteristics in the zonal and meridional direction can be calculated independently. We use this approximation below to construct wave characteristics and waves paths.

b. Results

Even though the mean flow is significant relative to the phase speeds of the baroclinic modes, we use the resting vertical modes and focus on the first few bar-
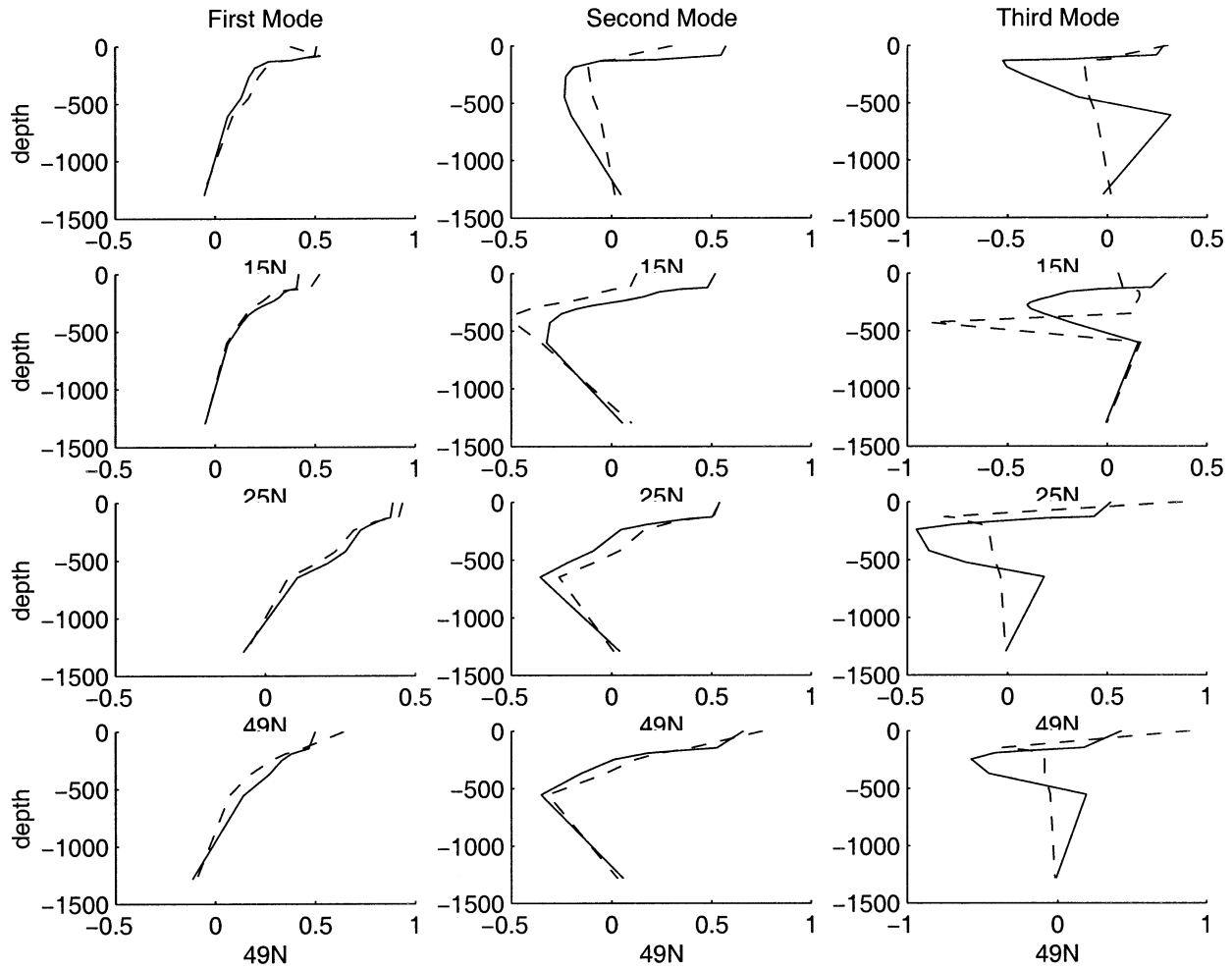
FIG. 1. Normalized modal structure of isopycnal displacement (eta) as a function of depth for the first three baroclinic modes at three different latitudes and 146°W. Solid line is the resting structure; dashed line is the structure calculated with zonal mean flow included.

oclinic modes. The advantage of using the resting vertical modes is that they are a complete and orthogonal set allowing any perturbation in the density (pressure) field to be described as a linear combination of the modes. In addition, the equations at rest are self-adjoint and diagonalizable. As noted above, the leading baroclinic mode is hardly affected by the mean flow and its separate dynamics should be captured by the projections. As we will show below, the results are surprisingly good, with different vertical modes showing distinct propagation characteristics that agree well with the linear analysis described above.

Given that any density perturbations can be described as a linear combination of the resting baroclinic modes, we can decompose the model density perturbations onto these baroclinic modes. The decomposition proceeds as follows: we write the streamfunction in any layer as a sum of contributions from each vertical mode. Using all of the modes, we can write at each point in time and at each latitude/longitude point

$$\Psi = \mathbf{Ra}, \tag{11}$$

where $\mathbf{R}$ is the matrix whose columns are made up of the eigenvectors, $\boldsymbol{\Phi}$, that represent the vertical structure of each mode and $\mathbf{a}$ is a vector that represents the magnitude of each mode and depends on time. The streamfunction normalization is $\sum_{k=1}^{k=n\mathrm{layers}} H_k \phi_{kn}^2 = 1$. Likewise, the normalization for the interface displacement is $\sum_{k=1}^{k=n\mathrm{layers}} g_k' \eta_{kn}^2 = 1$. The vector $\boldsymbol{\Psi}$ contains the model streamfunction as a function of time. During winter, when the interface depth anomalies are taken from the model, $\mathbf{a}$ is found from (11) and the model streamfunction deviations using

$$\mathbf{a} = \mathbf{R}^{-1}\boldsymbol{\Psi}. \tag{12}$$

The potential energy in each mode can be derived directly from $\mathbf{a}$.

Time–longitude plots of $\mathbf{a}$ from (12) for each vertical mode demonstrate that the decomposition separates out dynamically distinct modes of variability (Fig. 3) with
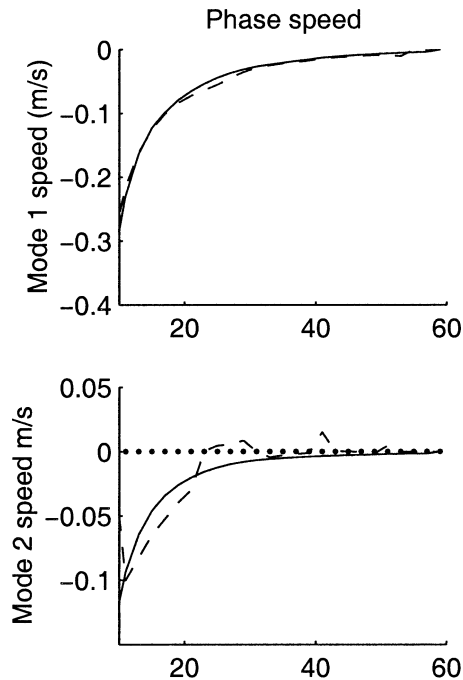
Phase speed

FIG. 2. Phase speed as a function of latitude at 146°W for the first three baroclinic modes. The solid line is the phase speed calculated with a resting ocean (m s⁻¹). The dashed line is the phase speed calculated with the zonal mean flow included. Notice the change of sign at midlatitudes for the second baroclinic mode.

the propagation speed noticeably different for each vertical mode. The zonal propagation speeds of each vertical mode do not agree with phase speed estimates from the calculation using a resting ocean. Instead, the zonal mean flow must be included to get good agreement. At each latitude, we generate a characteristic line by starting at the eastern (western) boundary and propagate to the west (east) using the phase speeds calculated when the zonal mean flow alone is included (Fig. 3). The agreement between the phase speed calculations and the propagation of the anomalies from the model is striking. At each latitude, westward phase speed decreases with mode number, and for the higher vertical modes, the phase speed reverses direction farther poleward. The least convincing comparison occurs at low latitudes. This can be blamed on the aliasing that occurs because we are only sampling once a year; at this latitude the Rossby waves travel fast enough that more frequent sampling is warranted. In addition, at low latitudes the Rossby wave is forced throughout the basin, which can result in an apparent phase speed that is faster than would be predicted from a free wave (Qiu et al. 1997).

The first baroclinic mode is primarily associated with the wind-driven circulation adjustment. The spatial distribution of the rms modal amplitude of the baroclinic mode (Fig. 4a) shows westward intensification and an increase in the subpolar gyre. The westward intensification results not only by a slight increase in the forcing in the west, but also because the amplitude of the Rossby

wave accumulates along the characteristics as the waves propagate to the west. This also results in westward intensification as would be found with the Sverdrup solution. The spatial structure is similar to that seen by Vivier et al. (1999) in an analysis of primarily annual Rossby waves from the Ocean Topography Experiment (TOPEX)/Poseidon altimetric observations. There is also a local maximum along 15°N and 10°S, associated with the intertropical convergence zones and the wind variability there. This maximum is associated with the Ekman pumping signal also described by Viver et al. Capatondi and Alexander (2001) also note that variability at 10°–15°N is associated with adiabatic (Rossby wave) displacements of the thermocline. Lysne and Deser (2002) note a maximum at 10°S in their analysis of model thermocline displacements as well.

The second baroclinic mode is maximum in a swath heading southwest from the date line in the Kuroshio Extension, with another local maximum centering at 140°W about the equator. The energy in the third baroclinic mode is maximum farther to the east in the Kuroshio Extension, with a hint of a propagation pathway to the southwest and another local maximum at 25°N and 140°W (not shown). The second and third baroclinic modes sample different parts of the water column, with the third-baroclinic-mode maximum slightly shallower than the second baroclinic mode. The maximum in the central Pacific for the second and third baroclinic modes reflects the subduction maximum associated with the formation of central mode water (Ladd and Thompson 2000). The local maximum farther to the east reflects the formation region of the eastern Subtropical Mode Water (Ladd and Thompson 2000; Hautala and Roemmich 1998).

Using (10), we calculated the wave characteristics for the zonal and meridional wavenumbers independently, assuming that the phase speeds are larger than the mean flow. The wave characteristics for the first baroclinic mode are generally westward in the subtropical gyre, modified slightly by the eastward flow in the Kuroshio Extension (Fig. 4a). The energy and wave characteristic paths are mostly consistent, with the forcing of the first baroclinic mode occurring in the central to western Pacific. The second baroclinic mode characteristics follow the subduction pathway as predicted by Liu (1999a) (Fig. 4b). The third baroclinic mode has a similar structure with slightly slower westward propagation (not shown). The higher baroclinic mode evolution is most likely suspect because the resting vertical structure no longer is a good approximation to the vertical structure in the presence of mean flow.

The basinwide averaged energy in the baroclinic modes is maximum for the first baroclinic mode, and falls off for the higher modes as expected, although the energy is comparable for the second and third baroclinic modes (Fig. 5). This suggests that the first and second baroclinic mode should at a minimum be included in analysis of decadal variability in the North Pacific.
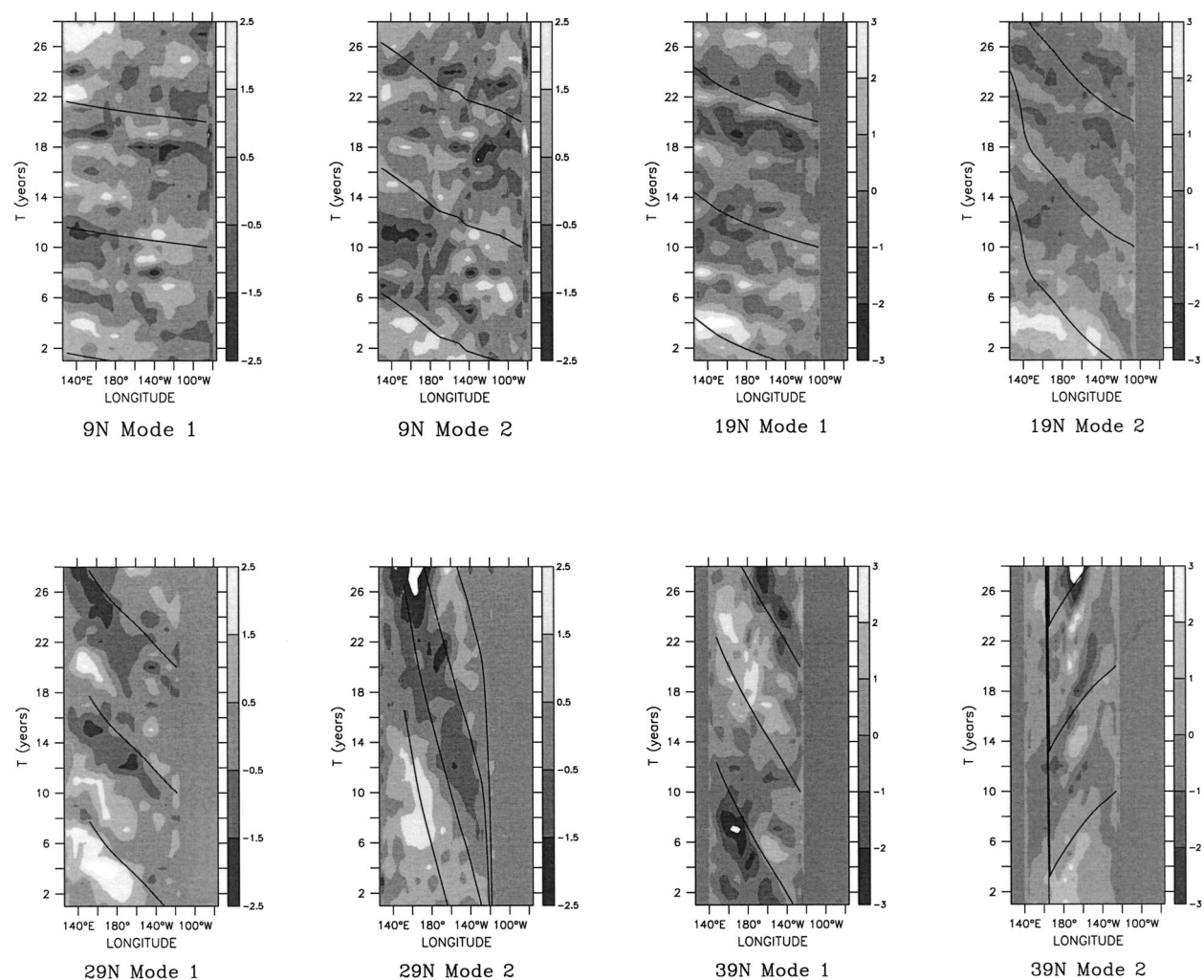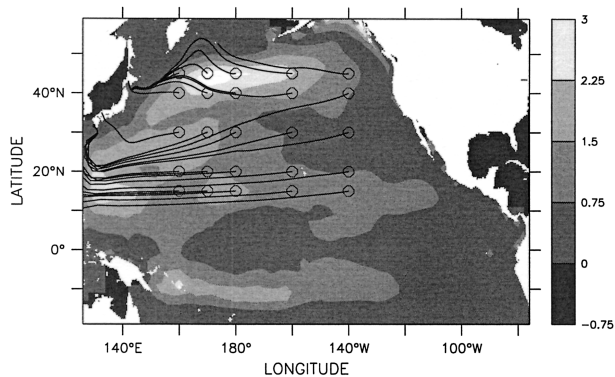
FIG. 3. Time–longitude plot for the amplitude of the first two baroclinic modes at four different latitudes (m). Overlain on top are wave characteristics calculated with the zonal mean flow included.

Two additional numerical model runs were done to evaluate the relative roles of thermodynamics and Ekman pumping in forcing the baroclinic modes. In run 2, the Ekman pumping was fixed to the climatological value, but the SST restoration and heat fluxes had interannual variability. In run 3, the SST restoration and heat fluxes were fixed to climatology while the winds had interannual variability. In run 2, the first baroclinic mode was less energetic than in the full run while the higher modes were nearly as large, which suggests that the higher baroclinic modes are dominantly forced by thermodynamics. Conversely, in run 3 the first baroclinic mode was larger than in run 2 or even the full run, and the higher modes were suppressed slightly. This suggests that Ekman pumping and diabatic pumping can destructively interfere with each other to give a smaller-than-expected first-baroclinic-mode response (Fig. 5).
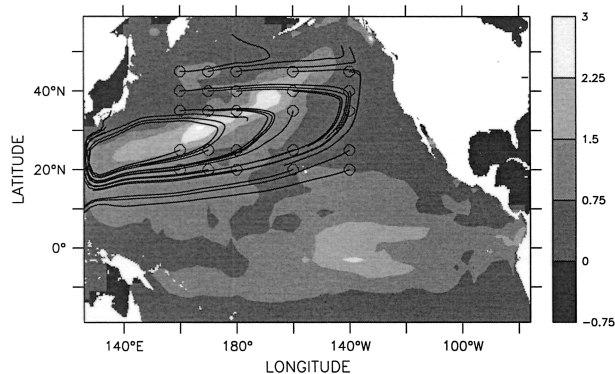
4. Forcing of the baroclinic modes

To understand how the thermocline variability is forced, we use quasigeostrophic theory following the method of Thompson et al. (2002) outlined below. We assumed that the motion is linear and has large horizontal length scales so that the relative vorticity can be ignored. In addition, we assumed that the mean flow is negligible. This last assumption is not strictly valid, as shown in section 3b. However, the analysis gives a qualitative picture of how the variability in each mode is forced.

The potential vorticity (PV) equations for each vertical mode can be derived in the layered framework. Mixing is written as a diapycnal flux at the top and bottom of each layer. The linear layer quasigeostrophic PV equations can be written

Mode 1 amplitude

RMS amplitude versus mode number

FIG. 5. Area-averaged rms amplitude as a function of mode number (m). Solid line is the control run, dotted line is run 2, and dashed line is run 3.

Mode 2 amplitude

FIG. 4. Rms amplitude in the first and second baroclinic modes (m). Overlain are wave characteristic paths calculated including the zonal and meridional mean flow separately. The open circles are the starting points of the characteristics, and each path represents 10 years of wave propagation.

$$\frac{\partial}{\partial t}\left(\frac{\psi_2 - \psi_1}{H_1 g_1} - \frac{\psi_1}{H_1 g}\right) + \beta\frac{\partial\psi_1}{\partial x} = \frac{f}{H_1}(w_{\text{Ek}} - w_1) \quad (13)$$

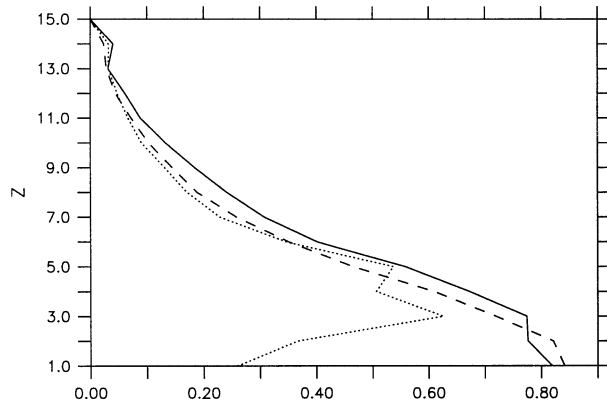for layer 1,

$$\frac{\partial}{\partial t}\left(\frac{\psi_{n+1} - \psi_n}{H_n g_n} + \frac{\psi_{n-1} - \psi_n}{H_n g_{n-1}}\right) + \beta\frac{\partial\psi_n}{\partial x}$$

$$= \frac{f}{H_n}(w_{n-1} - w_n) \quad (14)$$

for interior layers, and

$$\frac{\partial}{\partial t}\left(\frac{\psi_{m-1} - \psi_m}{H_m g_{m-1}}\right) + \beta\frac{\partial\psi_m}{\partial x} = \frac{f}{H_m}w_{m-1} \quad (15)$$

for the bottom layer. Here, w_n is the diabatic velocity or flux across the interface at the bottom of layer n. The diabatic vertical velocity w_n is maximum at the base of

the mixed layer and is generally small elsewhere in the water column. It represents the net flux of mass from (to) the mixed layer to (from) the thermocline.

The PV equations for each layer (13)–(15) can be written in matrix form as

$$\mathbf{L}\frac{\partial\mathbf{\Psi}}{\partial t} + \beta\frac{\partial\mathbf{\Psi}}{\partial x} = \mathbf{F}, \quad (16)$$

where $\mathbf{\Psi}$ is a vector representing the streamfunction in each layer and $\mathbf{F}$ is the rhs of (13)–(15).

Then (16) can be transformed to PV equations for each vertical mode (see Thompson et al. 2002 for details):

$$-\mathbf{C}\mathbf{R}^{\text{T}}\mathbf{H}\frac{\partial\mathbf{\Psi}}{\partial t} + \beta\mathbf{R}^{\text{T}}\mathbf{H}\frac{\partial\mathbf{\Psi}}{\partial x} = \mathbf{R}^{\text{T}}\mathbf{H}\mathbf{F}, \quad (17)$$

where $\mathbf{C}$ is a square matrix containing the eigenvalues (c^{-2}) from (6) as diagonal elements and $\mathbf{H}$ is a square matrix that contained the thicknesses of each layer as its diagonal elements. Next, we multiply (17) by $\mathbf{C}^{-1}$ to get

$$-\mathbf{R}^{\text{T}}\mathbf{H}\frac{\partial\mathbf{\Psi}}{\partial t} + \beta\mathbf{C}^{-1}\mathbf{R}^{\text{T}}\mathbf{H}\frac{\partial\mathbf{\Psi}}{\partial x} = \mathbf{C}^{-1}\mathbf{R}^{\text{T}}\mathbf{H}\mathbf{F}. \quad (18)$$

We have created an equation that defines the propagation and forcing of the potential vorticity for each vertical mode in terms of the vertical divergences ($\mathbf{F}$). The jth element of $\mathbf{R}^{\text{T}}\mathbf{H}\mathbf{\Psi}$ is the potential vorticity of the jth vertical mode that propagates with phase speed $\beta\mathbf{C}_j^{-1}$. We continue to assume that $\mathbf{R}$ and $\mathbf{H}$ are independent of time and vary slowly in the zonal direction.

In order to compare the diapycnal pumping against the Ekman pumping in magnitude and spatial distribution, we examined w_1, the diapycnal pumping across the base of the mixed layer. The rms Ekman pumping and rms w_1 have very different spatial patterns (Fig. 6). The Ekman pumping is fairly uniformly distributed over
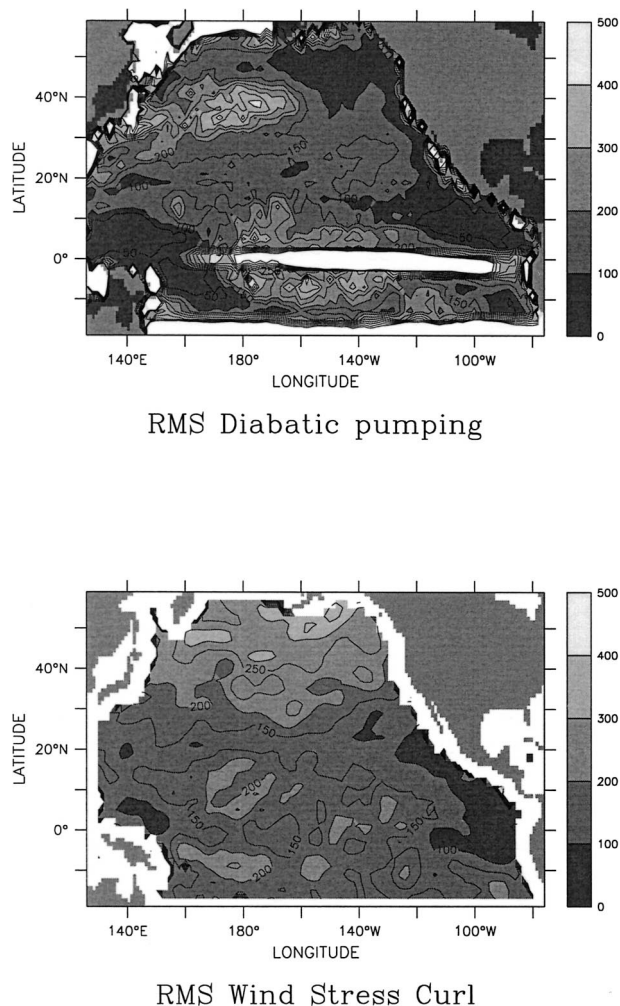
RMS Diabatic pumping

RMS Wind Stress Curl

FIG. 6. Rms diapycnal pumping (m s^{-1}, diapycnal vertical velocity out of the base of the mixed layer) scaled by 1×10^8 and Ekman pumping (m s^{-1}, scaled by 1×10^{10} in meters per second).

the basin, while the diabatic pumping is maximum in the subduction region of the Kuroshio Extension, where water is transferred to the thermocline, and at the equator, where this water is returned to the surface (Ladd and Thompson 2001). In addition, the forcing from Ekman pumping and diabatic pumping projects onto different parts of the water column. Ekman pumping occurs at the base of the Ekman layer, which in (17) we assume is a shallow layer located at the surface. The diabatic pumping is closely related to the subduction velocity, a velocity that described the transfer of mass between the mixed layer and the isopycnal layer below during the subduction window, which occurs over a period of 2 months in the late winter/early spring (Marshall et al. 1993). Thus, the two vertical velocities act on different parts of the water column, and the amplitude of the response depends not only on the forcing size but also on the vertical structure of the baroclinic mode of interest.

The decomposition of the forcing onto the PV equation for the different baroclinic modes (Fig. 7) shows that the spatial distribution of decomposed forcing fields is generally consistent with the energy in each mode, calculated as the rhs of (18) for each vertical mode. The patterns depend critically on where in the water column the forcing terms act. Since the diabatic pumping is very intermittent with the largest signal occurring in late winter (not shown), the diabatic pumping occurs predominantly at the base of the winter mixed layer in an annual mean. For the Ekman pumping, it is more uniformly distributed throughout the year. Since the model does not directly calculate Ekman pumping, we assume that it acts at the surface. Another equally valid assumption would be that it acts at the depth of the mean mixed layer. While quantitative differences come about because of this assumption, our qualitative conclusions do not depend on this assumption. The Ekman pumping is maximum for the first baroclinic mode and falls off uniformly with mode number (Fig. 8). Note that Ekman pumping does force the higher modes; quasigeostrophic dynamics shows that the amplitude of the mode is proportional to the inverse of the mode number squared for constant stratification and Ekman pumping acting at the surface. Diabatic pumping is large for modes 2 through 4. In addition, the spatial maximum in the energy can be understood from the forcing distribution. For the first baroclinic mode, the local maximum in Ekman pumping at 10°S and 10°N are reflected in the energy. At midlatitudes, the energy in mode 1 is maximum farther to the west than the Ekman pumping, reflecting the westward propagation of energy via Rossby waves. The diapycnal pumping also forces this mode in the eastern part of the Kuroshio Extension but destructively interferes with the Ekman pumping response, as was seen in the comparison between the different model runs.

For the second baroclinic mode, Ekman pumping is significantly smaller, with maxima in the northeast Pacific and at 10°N and 10°S, straddling the equator (Fig. 7). The tropical maximum is reflected in the energy of mode 2 (Fig. 4). Diapycnal pumping plays a dominant role at midlatitudes and forces the energy maxima that begins in the Kuroshio Extension and travels southwest to the western boundary. In contrast to the first baroclinic mode, the diabatic pumping constructively interferes with the Ekman pumping. There is a very weak local diapycnal forcing maximum in the eastern subtropics (it is more apparent in the third-baroclinic-mode forcing but is not shown here), as depicted in the idealized runs of Liu (1999a), but the larger maximum is farther to the west. This maximum is consistent with large changes in the CMW region seen by Ladd and Thompson (2002) in the same model run and in a similar run by Xie et al. (2000). Variability in the Tropics is much more closely tied to the local Ekman pumping, confirming the conclusions of Schneider et al. (1999) that tropical variability in the thermocline is controlled by tropical winds.
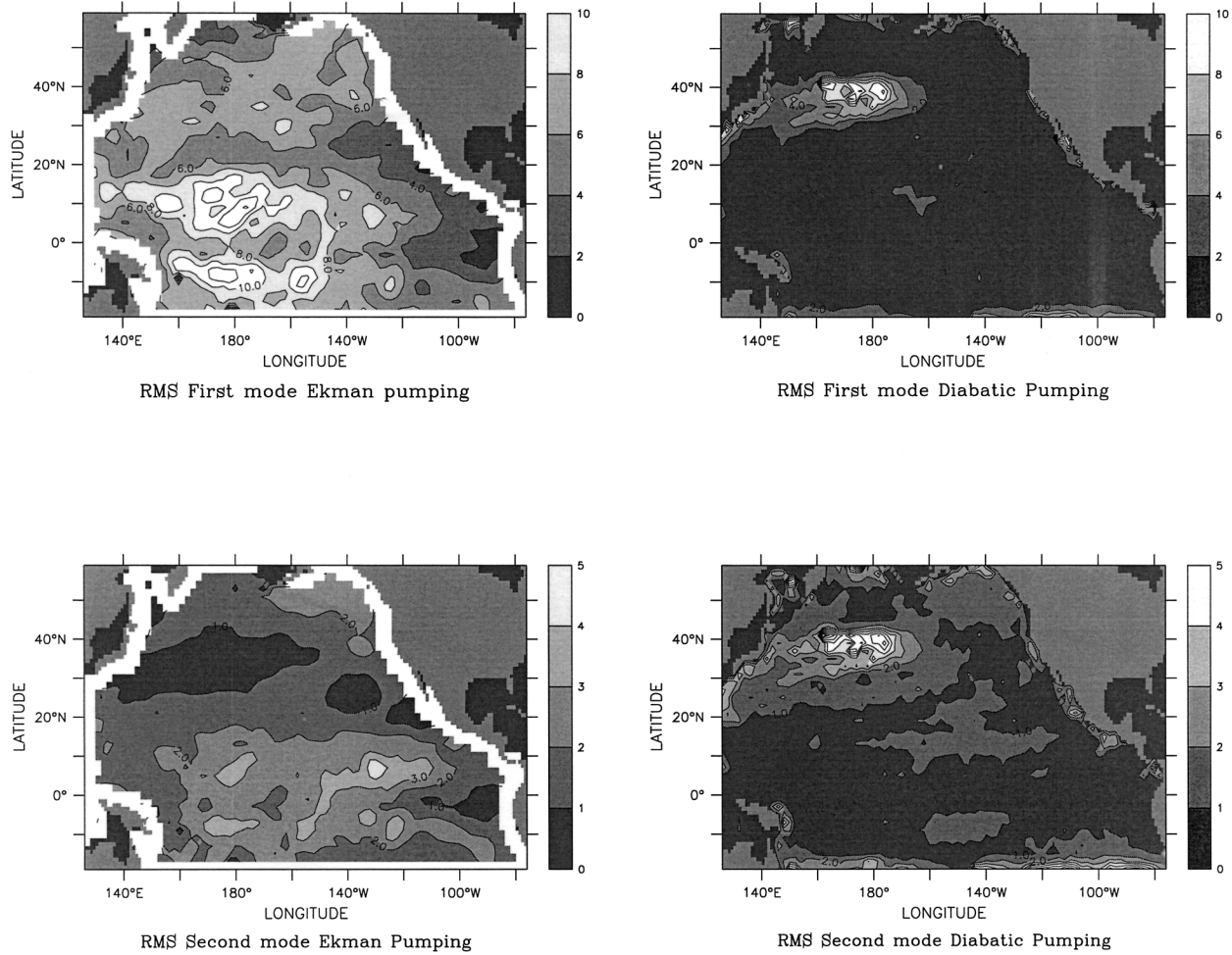
FIG. 7. Rms Ekman pumping and diapycnal pumping forcing for the first two baroclinic modes as taken from (17) in units of inverse meters. Notice the change in scale.
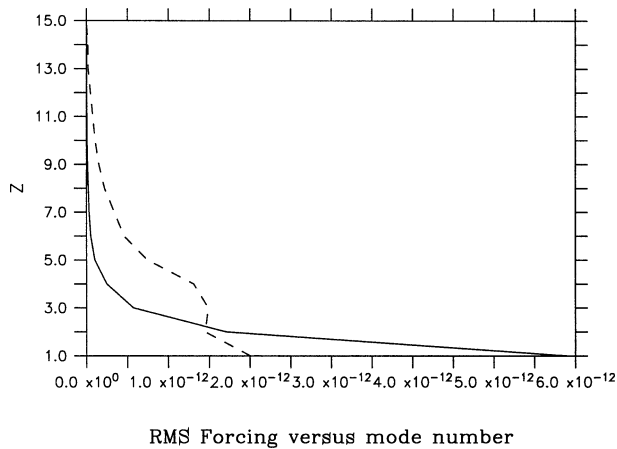

FIG. 8. Area-averaged rms Ekman pumping (solid) and diapycnal pumping (dashed) forcing as a function of mode number.

5. Mode coupling

There is also coupling between the modes in the presence of mean flow. To get an estimate for the amount of mode coupling that occurs, we return to the potential vorticity equation (16). We expand the streamfunction into a sum of the resting vertical modes $\psi = \Sigma_{n=1}^3 b_n \phi_n$, where we truncate at mode 3 and ϕ_n is the vertical structure of the nth internal mode and b_n is its amplitude that varies with longitude and time. The nth baroclinic mode amplitude can be scaled by c_n^2 from the Ekman pumping response. We rewrite the streamfunction as $\psi = \Sigma_{n=1}^3 c_n^2 a_n \phi_n$. Then (16) becomes, assuming zonal mean flow only,

$$\frac{\partial}{\partial t}\left(\sum_{n=1}^3 c_n^2 a_n q_n\right) + U\frac{\partial}{\partial x}\left(\sum_{n=1}^3 c_n^2 a_n q_n\right)$$

$$+ \overline{q}_y \frac{\partial}{\partial x}\left(\sum_{n=1}^3 c_n^2 a_n \phi_n\right) = F, \qquad (19)$$

where the rhs is given by the forcing in (16) and q_n is

the potential vorticity of the *n*th vertical mode. Then (6) enables us to rewrite (19) as

$$\frac{\partial}{\partial t}\left(\sum_{n=1}^{3} f^2 a_n \phi_n\right) + U\frac{\partial}{\partial x}(f^2 a_n \phi_n)$$

$$+ \overline{q}_y\frac{\partial}{\partial x}\left(\sum_{n=1}^{3} a_n c_n^2 \phi_n\right) = F. \qquad (20)$$

We construct the evolution equation for the first baroclinic mode by multiplying by its vertical structure and integrating in depth. Since the modes are orthogonal and normalized, we have

$$\frac{\partial}{\partial t}(f^2 a_1) + \frac{\partial}{\partial x}\left(\sum_{n=1}^{3} f^2 a_n \int_{z=-H}^{0} dz U\phi_1\phi_n\right)$$

$$+ \frac{\partial}{\partial x}\left(\sum_{n=1}^{3} a_n \int_{z=-H}^{0} dz \overline{q}_y c_n^2 \phi_1\phi_n\right) = F. \qquad (21)$$

We have made the WKB assumption once again and assumed that the mean flow has no zonal variations. We then get an evolution equation for a_1 as in (18):

$$\frac{\partial a_1}{\partial t} + \frac{\partial a_1}{\partial x}\int_{z=-H}^{0} dz\left(U + \frac{c_1^2 \overline{q}_y}{f^2}\right)\phi_1^2$$

$$+ \frac{\partial a_2}{\partial x}\int_{z=-H}^{0} dz\left(U + \frac{c_2^2 \overline{q}_y}{f^2}\right)\phi_1\phi_2$$

$$+ \frac{\partial a_3}{\partial x}\int_{z=-H}^{0} dz\left(U + \frac{c_3^2 \overline{q}_y}{f^2}\right)\phi_1\phi_3 = \frac{F}{f^2}. \qquad (22)$$

An equivalent equation can be derived for the second baroclinic mode. As a measure of the influence of the coupling of the second to the first baroclinic mode, we calculate the ratio of the second integral on the lhs relative to the third integral on the lhs. The influence of the second baroclinic mode on the evolution of the first baroclinic mode can be measured by

$$\Gamma_{12} = \frac{c_2^2}{c_1^2}\frac{\int_{z=-H}^{0} dz(U + c_2^2 \overline{q}_y/f^2)\psi_1\psi_2}{\int_{z=-H}^{0} dz(U + c_1^2 \overline{q}_y/f^2)\psi_1^2}. \qquad (23)$$

Likewise, we can define Γ_{13}. For the second baroclinic mode we define Γ_{21}, and Γ_{23} in an equivalent manner. The third baroclinic mode has little influence on the propagation of the lower modes (not shown). On the other hand, there is potential for significant coupling in the return flow of the subtropical gyre where the values of Γ_{12} and Γ_{21} are significantly greater than 1 (Fig. 9). This is the region where Liu (1999b) identified in a 2½-layer quasigeostrophic model a ''Green mode'' that occurs as a long unstable wave that can be described as a combination of his ''N'' mode and his ''A'' mode. This instability implies coupling between the two
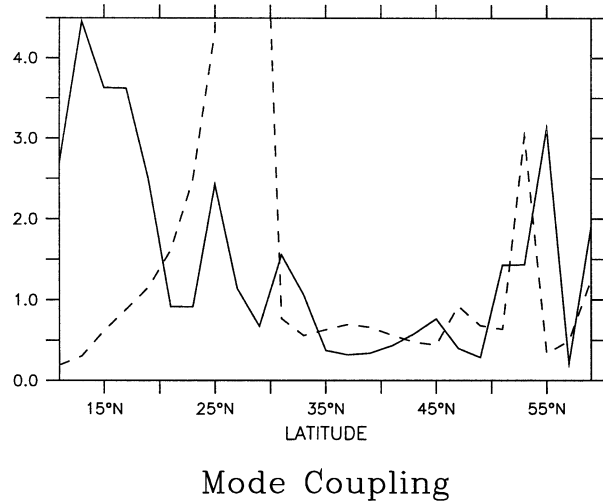

Mode Coupling

FIG. 9. Amount of mode-2 influence on mode-1 evolution given by Γ_{12} as defined in (23) (solid), and mode-1 influence on mode-2 propagation given by Γ_{12} (dashed).

modes. For the first baroclinic mode, the maximum coupling occurs in the western Pacific between 20° and 30°N (the location of the Green mode) and along 15°N. We showed earlier that the propagation is least distinct at 9° and 19°N (Fig. 3) for both first and second baroclinic modes, which is consistent with the presence of mode coupling (and potential long-wave instability). The regions where mode coupling is large call into question the validity of the modal decomposition in those regions.

6. Connection between forcing and mode evolution

To complete the analysis and to understand the distribution of energy in each baroclinic mode more completely, we return to the potential vorticity equation [(18)] and use the derived forcing fields to find the linear long-wave response. To do this, we use the zonal phase speed derived by from (8) and substitute this into (17) to get a one-dimensional wave equation for the propagation of forced Rossby waves. We use the zonally averaged phase speed at each latitude and only integrate north of 10°N, where we expect quasigeostrophic theory to be valid. For simplicity, we ignore meridional propagation. This is similar to the calculation done by Sturges and Hong (1995) for wind forcing only. A time series of the one-dimensional wave equation response in the Kuroshio Extension confirms the destructive interference between the wind forced and diabatic forced response (Fig. 10). This also may be consistent with the notion that wind-driven temperature anomalies are damped by air–sea fluxes of heat in the Kuroshio region (Xie et al. 2000). However, a detailed analysis of the influence of the different baroclinic modes on the SST budget would have to be done before this was confirmed.
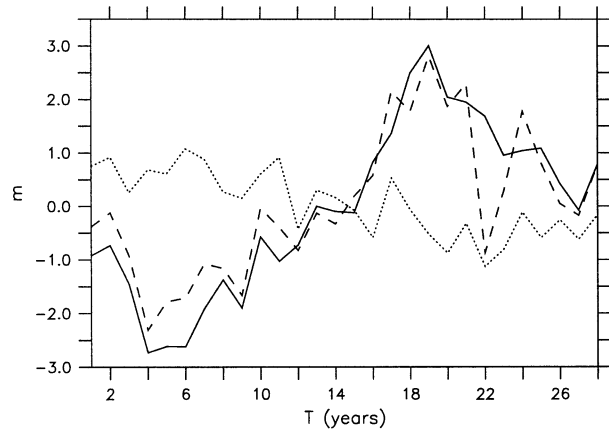
Mode one amplitude

FIG. 10. Time series at 40°N, 180° for the first baroclinic mode response from Ekman pumping (solid), diabatic pumping (dashed), and total (dotted).

The rms potential energy distribution from the Ekman pumping and diabatic pumping work to explain the sum of the spatial patterns of the total energy in the first and second baroclinic modes (cf. Fig. 11 to Fig. 4). The first-baroclinic-mode response forced by Ekman pumping shows maxima at 15°, 30°, and 45°N, all of which are also reflected in the total energy of the first baroclinic mode (although note that the amplitudes are larger in the wave equation response than in the numerical model response). The western intensification is well predicted by the one-dimensional model.

The influence of meridional propagation explains some of the discrepancies between the fields shown in Fig. 11 and Fig. 4, with the wave equation giving patterns that are more zonal than the numerical model fields where a suggestion of meridional propagation particularly west of the date line can be seen.

For the second baroclinic mode, the amplitudes are reasonably well estimated, with maxima at 40° and 30°N. The neglect of meridional propagation is more serious here. The amplitude as a function of latitude is

Mode 1 amplitude from Ekman pumping

Mode 1 amplitude from diabatic pumping

Mode 2 amplitude from Ekman pumping

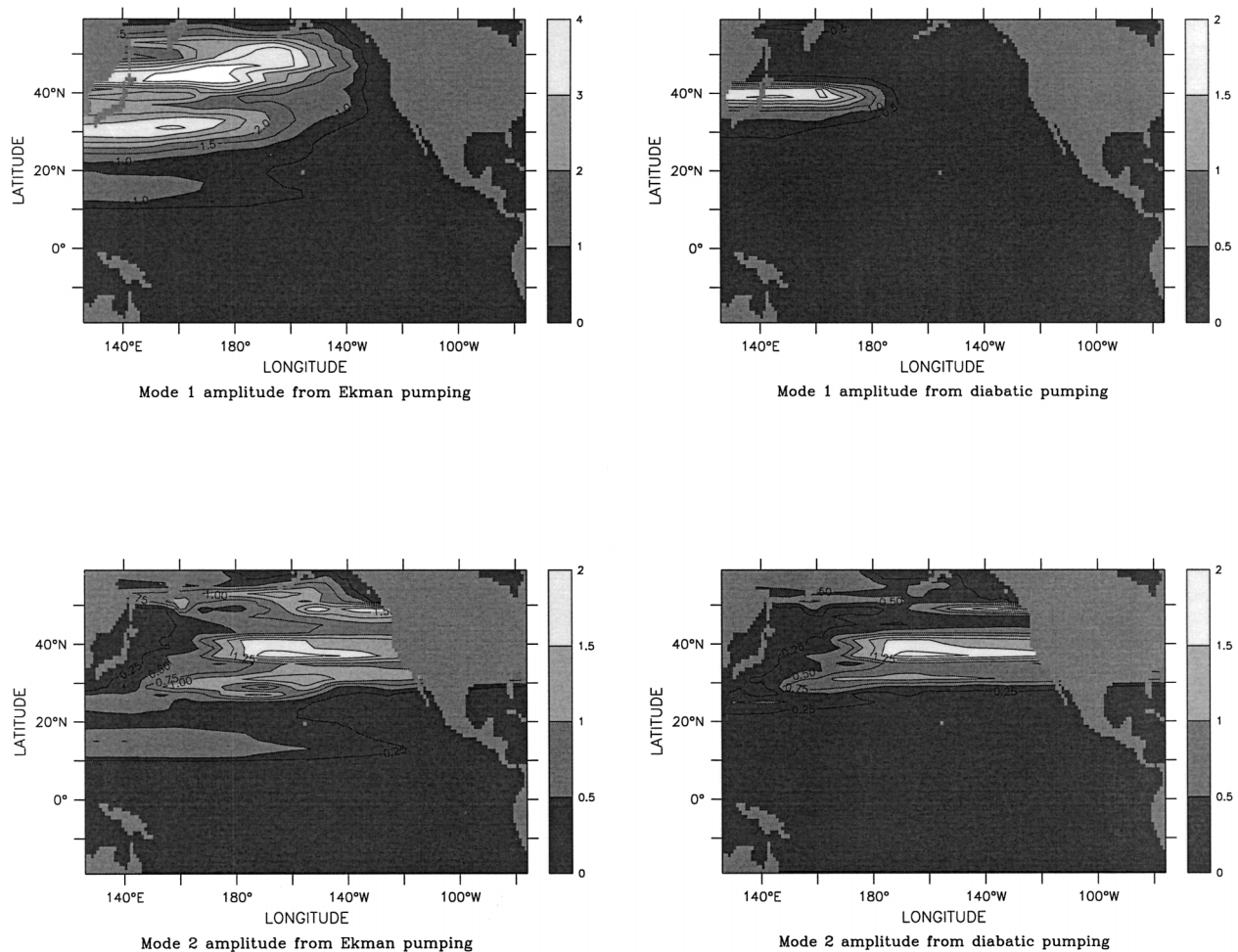Mode 2 amplitude from diabatic pumping

FIG. 11. Rms amplitude of the first and second baroclinic mode response from Ekman pumping and diabatic pumping (m). Note the change in color scale. South of 10°N, the energy is not calculated owing to the inadequacy of quasigeostrophic theory in the Tropics.

well reproduced with the Ekman pumping and diabatic pumping supplying about equal amounts of forcing. We also predicted this from runs 2 and 3 (Fig. 5) where the total response is about the sum of the response from Ekman pumping alone and heating alone.

7. Conclusions

A modal analysis applied to a multidecadal numerical simulation of the North Pacific demonstrates a decomposition of the variability of the thermocline into dynamical vertical modes. The different vertical modes separate distinct modes of variability, as can be seen from their different propagation characteristics. The method works because, for the low baroclinic modes, the vertical structure is not very sensitive to the presence of the mean flow. In addition, the resting vertical modes are orthogonal and complete, and so they provide a consistent way of decomposing the motions. The propagation characteristics, however, can only be understood when the presence of the mean flow is taken into account in the phase speeds. The linear analysis works surprisingly well, with the energy in each mode qualitatively consistent with the forcing of each mode. The propagation characteristics also agree reasonably well with the analysis including both zonal and meridional mean flow, although the wave paths should only be taken as approximate considering the assumptions made in the analysis. Each mode is forced in distinct locations with the first baroclinic mode forced throughout the basin, while the second baroclinic mode is mostly forced in the Kuroshio Extension with additional forcing in the Tropics.

As predicted by Liu (1999a), thermocline variability comes from both the first-baroclinic-mode response (mostly forced by Ekman pumping, but significantly influenced by diapycnal pumping) as well as a second-baroclinic-mode response (forced by both Ekman and diapycnal pumping). At the same time, the third baroclinic mode should not be ignored, particularly at mid- to high latitudes. The energy in the modes is consistent with the Schneider et al. (1999) result that the variability in the tropical thermocline results from forcing in the Tropics, and not from subduction anomalies in the midlatitudes. The results also show the distinctive westward-propagation response suggested by the Latif and Barnett (1996) analysis, although it is more complex than originally envisioned. In particular, the wind-driven response can be either suppressed or enhanced by the thermodynamics (or diabatic) response.

The dynamical response of the midlatitude thermocline to diapycnal pumping clarifies the connection between mode water changes, subduction, and thermocline variability. Diapycnal pumping, or the flux of mass out of the base of the mixed layer, is closely related to the subduction rate as defined by Marshall et al. (1993) (see also Ladd and Thompson 2001). As the subduction rate varies, the thermocline responds dynamically, and

anomalies propagate along the subduction pathway as proposed by Liu (1999a) and described by Ladd and Thompson (2002) in addition to modifying the first-baroclinic-mode response.

This work suggests that the second mode should be considered along with the first in modeling thermocline variability. The different propagation pathways for the modes complicate the response; in particular, the advective pathways cannot be ignored in considering how the thermocline responds to changes in forcing. We showed that the first- and second-baroclinic-mode structure is relatively insensitive to the presence of the mean flow, especially in regions away from large mode coupling (and instability). The higher modes are more problematic, especially in regions of high mean flow. Where the mean flow is strong, it is questionable whether the second and third modes can be distinguished from one another.

The questions remains as to why the modal decomposition works as well as it does. As suggested by Liu (1999a), the presence of mean shear modifies the phase speed of the baroclinic mode but does not substantially modify the vertical structure. As one moves to the higher vertical modes, the mean flow becomes more important in their propagation, as was shown to be true for the second baroclinic mode. The projection of the isopycnal displacements onto the baroclinic modes take advantage of the different behavior between the first and higher modes. As noted by Wunsch (1997) in his modal decomposition of mooring observations in the World Ocean, the modal decomposition has the advantage over, say, EOFs in that it keeps keep dynamically distinct feature separate. EOFs end up mixing the different vertical modes together, and only work well when their energy levels are very different. In the case of interannual to decadal variability in the midlatitudes, the different vertical modes have similar energy levels, and probably could not be separated by traditional EOF analysis.

In this analysis, we have ignored the possibility of spiciness (the generation of temperature and salinity anomalies in the thermocline), and we plan on redoing the analysis with a model run that includes the nonlinear equation of state and separate effects of temperature and salt. Additional analysis must be done to determine the impacts of the baroclinic modes on the sea surface temperature and heat content anomalies. Latif and Barnett (1996) suggest that the heat content anomaly should propagate as the first baroclinic mode. Based on the analysis presented here, we expect that description of heat content anomaly propagation should include at least the first two baroclinic modes.

REFERENCES

Capotondi, A., and M. A. Alexander, 2001: Rossby waves in the tropical North Pacific and their role in decadal thermocline variability. *J. Phys. Oceanogr.,* **31,** 3496–3515.

Deser, C., M. A. Alexander, and M. S. Timlin, 1996: Upper-ocean thermal variations in the North Pacific during 1970–1991. *J. Climate,* **9,** 1840–1855.

——, ——, and ——, 1999: Evidence for a wind-driven intensification of the Kuroshio current extension from the 1970s to the 1980s. *J. Climate,* **12,** 1697–1706.

Frankignoul, C., C. Duchene, and E. Zorita, 1997: A simple model of the decadal response of the ocean to stochastic wind forcing. *J. Phys. Oceanogr.,* **27,** 1533–1546.

Gu, D., and S. G. H. Philander, 1997: Interdecadal climate fluctuations that depend on exchanges between the tropics and extratropics. *Science,* **275,** 805–810.

Hallberg, R., 2000: Time integration of diapycnal diffusion and Richardson number dependent mixing in isopycnal coordinate ocean models. *Mon. Wea. Rev.,* **128,** 1402–1419.

——, and P. Rhines, 1996: Buoyancy-driven circulation in an ocean basin with isopycnals intersecting the sloping boundary. *J. Phys. Oceanogr.,* **26,** 913–940.

Hautala, S. L., and D. H. Roemmich, 1998: Subtropical mode water in the Northeast Pacific Basin. *J. Geophys. Res.,* **103,** 13 055–13 066.

Killworth, P. D., and J. R. Blundell, 1999: The effect of bottom topography on the speed of long extratropical planetary waves. *J. Phys. Oceanogr.,* **29,** 2689–2710.

——, and ——, 2001: Large-scale propagating disturbances: Approximation by vertical normal modes. *J. Phys. Oceanogr.,* **31,** 2852–2870.

——, D. B. Chelton, and R. A. deSzoeke, 1997: The speed of observed and theoretical long extratropical planetary waves. *J. Phys. Oceanogr.,* **27,** 1946–1966.

Ladd, C. A., and L. Thompson, 2000: Formation mechanisms for North Pacific central and eastern subtropical mode waters. *J. Phys. Oceanogr.,* **30,** 868–887.

——, and ——, 2001: Water mass formation in an isopycnal model of the North Pacific. *J. Phys. Oceanogr.,* **31,** 1517–1537.

——, and ——, 2002: Decadal variability of North Pacific Central Mode Water. *J. Phys. Oceanogr.,* **32,** 2870–2881.

Latif, M., and T. P. Barnett, 1994: Causes of decadal climate variability over the North Pacific and North America. *Science,* **266,** 634–637.

——, and ——, 1996: Decadal climate variability over the North Pacific and North America: Dynamics and predictability. *J. Climate,* **9,** 2407–2423.

Liu, Z., 1999a: Forced planetary wave response in a thermocline gyre. *J. Phys. Oceanogr.,* **29,** 1036–1055.

——, 1999b: Planetary wave modes in the thermocline: Non-Doppler-shift mode, advective mode and Green mode. *Quart. J. Roy. Meteor. Soc.,* **125,** 1315–1339.

Lysne, J., and C. Deser, 2002: Wind-driven thermocline variability in the Pacific: A model–data comparison. *J. Climate,* **15,** 829–845.

Mantua, N. J., S. R. Hare, Y. Zhang, J. M. Wallace, and R. C. Francis, 1997: A Pacific interdecadal climate oscillation with impacts on salmon production. *Bull. Amer. Meteor. Soc.,* **78,** 1069–1079.

Marshall, J. C., A. J. G. Nurser, and R. G. Williams, 1993: Inferring the subduction rate and period over the North Atlantic. *J. Phys. Oceanogr.,* **23,** 1315–1329.

Qiu, B., W. Miao, and P. Muller, 1997: Propagation and decay of forced and free baroclinic Rossby waves in off-equatorial oceans. *J. Phys. Oceanogr.,* **27,** 2405–2417.

Schneider, N., and A. J. Miller, 2001: Predicting western North Pacific ocean climate. *J. Climate,* **14,** 3997–4002.

——, ——, M. A. Alexander, and C. Deser, 1999: Subduction of decadal North Pacific temperature anomalies: Observations and dynamics. *J. Phys. Oceanogr.,* **29,** 1056–1070.

——, ——, and D. W. Pierce, 2002: Anatomy of North Pacific decadal variability. *J. Climate,* **15,** 586–605.

Seager, R., K. Yochanan, N. H. Naik, M. A. Cane, and J. Miller, 2001: Wind-driven shifts in the latitude of the Kuroshio–Oyashio Extension and generation of SST anomalies on decadal time-scales. *J. Climate,* **14,** 4249–4265.

Sturges, W., and B. G. Hong, 1995: Wind forcing of the Atlantic thermocline along 32°N at low frequencies. *J. Phys. Oceanogr.,* **25,** 1706–1715.

Thompson, L. K., A. Kelly, D. Darr, and R. Hallberg, 2002: Buoyancy and mixed layer effects on the Sea Surface Height Response in an isopycnal model of the North Pacific. *J. Phys. Oceanogr.,* **32,** 3657–3670.

Vivier, F., K. A. Kelly, and L. Thompson, 1999: The contribution of waves, wind forcing and surface heating to sea surface height observations of the North Pacific Ocean. *J. Geophys. Res.,* **104,** 20 767–20 784.

Wunsch, C., 1997: The vertical partition of oceanic horizontal kinetic energy. *J. Phys. Oceanogr.,* **27,** 1770–1794.

Xie, S.-P., T. Kunitani, A. Kubokawa, M. Nonaka, and S. Hosoda, 2000: Interdecadal thermocline variability in the North Pacific for 1958–1997: A GCM simulation. *J. Phys. Oceanogr.,* **30,** 2798–2813.

Zhang, Y., J. M. Wallace, and D. S. Battisti, 1997: ENSO-like interdecadal variability: 1900–93. *J. Climate,* **10,** 1004–1020.